




3D microstructure of magnesium potassium phosphate ceramics from X-ray tomography: new insights into the reaction mechanisms

Alberto Viani^{1,*} , Konstantinos Sotiriadis¹, Gabriele Lanzafame², and Lucia Mancini²

¹Institute of Theoretical and Applied Mechanics of the Czech Academy of Sciences, Centre of Excellence Telč, Batelovská 485, 58856 Telč, Czech Republic

²Elettra-Sincrotrone Trieste S.C.p.A, SS 14- km 163.5, Area Science Park, 34149 Basovizza, Trieste, Italy

Received: 25 September 2018

Accepted: 7 November 2018

Published online:
12 November 2018

© The Author(s) 2018

ABSTRACT

Magnesium potassium phosphate ceramics are chemically bonded ceramics employed as biomaterials, in nuclear waste encapsulation and for concrete repair. The microstructure dictates material performance and depends on the raw mix composition. Synchrotron X-ray computed microtomography was employed to describe the 3D microstructure and its time evolution during hardening and gain insights into the reaction mechanisms. Any excess water with respect to the stoichiometry of the reaction brought about an increase in porosity, but, notably, a reduction in the average pore size. Crystals filled the water ‘pockets’ in the ceramic volume by growing larger, although less densely packed, increasing the complexity of the pore shape. Platelet over elongated crystal habit was favoured. Such a change in shape is likely related to a change in reaction mechanism, as crystallization from a gel-like amorphous precursor is hindered and progressively substituted by a through-solution mechanism. It is proposed that the time evolution of the microstructure is dictated by the balance between crystallization from amorphous precursor, prevailing in relatively ‘dense’ systems (with stoichiometric water or in low excess), and water segregation, prevailing at higher water contents. The former mechanism was shown to produce an increase in porosity with time, because of the density mismatch between the amorphous and the crystalline phase.

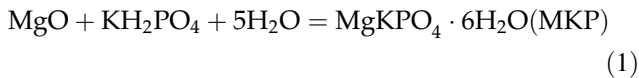
Introduction

Magnesium potassium phosphate ceramics (MPCs) set at room temperature through the aqueous reaction between basic MgO and an acid phosphate. They

have been employed as bioengineering materials [1], in dentistry as materials for dental investments [2], as cements for nuclear waste encapsulation [3] and in the rapid repair of concrete [4]. For the type of MPCs

Address correspondence to E-mail: viani@itam.cas.cz

studied in this work, the reaction is usually written as:



In order to optimize working time, rheological properties and performance, the influence of magnesia-to-phosphate molar ratio, water-to-solid weight ratio (w/s), grain size distribution and reactivity of MgO has been extensively studied [5–9]. The body of literature is far from systematic, due to the variation in the use of retarders, sand and aggregate fraction, and type of MgO [10]. Commonly, effective formulations contain an excess of MgO [11, 12], resulting in a molar ratio between MgO and potassium di-hydrogen phosphate (KH_2PO_4 , KDP) higher than 1. The first reaction product is amorphous/paracrystalline [13–15], and even if at $w/s = 5$ an intermediate phase ($\text{Mg}_2\text{KH}(\text{PO}_4)_2 \cdot 15\text{H}_2\text{O}$) has been detected, from 30 min on, the only crystalline phase present in the system is MKP [16]. The strength seems to be driven mostly by the progressive development of a network of elongated or tabular crystals of MKP in the ceramic volume [17, 18]. However, the time evolution of the microstructure should depend not only on crystallization of MKP, but also on the water content of the mix.

In principle, the optimal amount of water must satisfy Eq. 1; a lower content would leave a fraction of unreacted reagents and any excess should be segregated in pores within the volume. Studies on pastes and suspensions with large water contents have been frequently reported [16, 19–22], and Mg–P-based materials with excess of water have been considered for specific applications, like in the fabrication of injectable biomedical cements [23] (w/s up to 1). However, detailed characterization of the role of water in defining the microstructure in MPC is lacking. Quantitative data on the MPC microstructure have been obtained only from mercury intrusion porosimetry (MIP) and indicate that any increase in w/s ratio above the stoichiometric amount brings about an increase in porosity [7, 24, 25]. Moreover, MIP porosity was reported to decrease during the course of the reaction and with sample ageing (up to 28 days). This decrease interested mainly the fine porosity (diameter $D < 4 \mu\text{m}$ [7, 25] or $D < 0.12 \mu\text{m}$ [18]). For larger pores, the trend is less clear, and the results from the literature sometimes disagree (see for

example [7, 25]). Therefore, the concept of a progressively dense body, with lower total porosity and lower specific surface area of pores (S_V), employed in the formulation of predictive models [7], is still not supported by conclusive experimental evidences.

In general, it is of practical importance to verify the role of water on the development of the coarse microstructure of MPCs (up to mm in pore size), because it may help to shed light on the reaction mechanisms, and, ultimately, help in product design. In fact, different reaction sequences have been reported in function of MPC formulation [16, 20, 22, 26]. There is indication that this occurs in reason of the degree of supersaturation achieved in solution in the first stages of the reaction. High supersaturation drives the reaction towards kinetic control, dictating the relative amount and the nature of the amorphous and crystalline products, together with the crystal habit of MKP [26, 27].

In this work, we report on the three-dimensional (3D) quantitative image analysis of the pore structure in MPCs with different w/s ratio, based on results from phase-contrast synchrotron radiation computed microtomography (SR- μCT). SR- μCT allows for retrieving microscale information of the sample pore network in a fully non-destructive fashion [28, 29], overcoming some drawbacks of the MIP technique. For example, under the vacuum conditions needed for the MIP tests, the material loses a consistent fraction of structural water [13], a process common to other hydrated systems [30, 31], which invariably leads to the deterioration of the microstructure, impairing the accuracy of the results.

Materials and methods

MgO samples were obtained by calcining pharmaceutical grade MgCO_3 at 1600 °C for 40 min. The powder was milled for 2 min in a Mini-Mill Pulverisette 23 (Fritsch) at 30 oscillations/min and stored in desiccator until use. Particle size analysis was conducted in triplicate, resulting in a BET surface area of $0.9 \text{ m}^2 \text{ g}^{-1}$ and $d_{50} = 5.5 \mu\text{m}$. Water was added to mixtures of MgO and KDP with magnesia-to-phosphate molar ratio of 1.75 to attain w/s ratio of 0.44, 1.00, 2.07 and 4.00. The formulation with $w/s = 0.44$ is stoichiometric with respect to KDP, whereas 10.2 wt% of the mix will be unreacted MgO (supposing complete consumption of KDP, according

to Eq. 1). The pastes were produced at room temperature. After mixing for 20 s, the samples were casted in form of cylinders (3.8 mm diameter, \sim 20 mm height) and kept sealed in plastic bags at 20 °C until measurement. SR- μ CT data were collected after 15 days. In addition, in order to study the time evolution of the microstructure of a sample with water content slightly exceeding the stoichiometric amount, the 0.51 w/s ratio was chosen, and SR- μ CT data were collected at 1, 4, 9 and 12 h after mixing. None of the samples showed effects of water bleeding or inhomogeneities at the macroscopic, as well as at the scale of optical microscopy.

The naming convention adopted in this paper for the MPC samples is MPC_X_Y, where X identifies the w/s ratio (044, 051, 100, 207, 400) and Y the ageing time (1 h, 4 h, 9 h, 12 h and 15d).

Phase-contrast SR- μ CT measurements

High-resolution SR- μ CT data have been collected at the SYRMEP beamline of the Elettra Sincrotrone facility in Basovizza (Trieste, Italy). The cylindrical samples were covered with Parafilm M[®] to prevent water loss and mounted on a rotating stage. A filtered white X-ray beam (1.5 mm Si + 1 mm Al) was used to image the samples in local or region-of-interest mode [28]. In total, 1800 radiographic projections over a total angular range of 180° were acquired with an exposure time/projection of 1.5 s for the most stable samples MPC_044_15d, MPC_100_15d, MPC_207_15d and MPC_400_15d. To follow the time evolution of the microstructure (sample MPC_051_Y), 900 projections with an exposure time/projection of 1.0 s, were acquired.

The detector used was an air-cooled 16-bit sCMOS camera (Hamamatsu C11440-22C) with a 2048 \times 2048 pixel chip and an effective pixel size of 0.9 $\mu\text{m} \times$ 0.9 μm . In order to enhance the visibility of phases with similar linear attenuation coefficients and the pore edges, we worked in propagation-based phase-contrast mode, setting the sample-to-detector distance to 80 mm [32, 33].

The tomographic reconstruction of the SR- μ CT images was performed by the SYRMEP Tomo Project software developed at Elettra [34, 35], using the filtered back projection algorithm [36]. A single-distance phase-retrieval algorithm [37] was applied to the projection images in order to improve the reliability of quantitative morphological analysis and enhance the contrast between the pores and the solid. To this aim, the ratio

$\gamma = \delta/\beta$ between the real and imaginary parts of the refractive index in the samples has been optimized for each sample typology and ranged from 20 to 40.

Processing and analysis of SR- μ CT images

Processing and quantitative analysis of the reconstructed volumes were performed by means of Pore3D software library [38] (<http://www.elettra.eu/pore3D>) developed at Elettra. The freeware software Fiji [39] was adopted to visualize the reconstructed or processed bi-dimensional (2D) slices, while the commercial software VGStudio Max 3.0 (Volume Graphics) was employed for the 3D visualization by using volume rendering procedures.

For the purpose of this study, image segmentation was aimed at isolating the pores from the matrix of the sample, in order to obtain a binary image composed by voids and matrix. Pore edge recognition was facilitated by the application of an anisotropic diffusion filter [40]. Segmentation was then performed using the automatic Otsu's method [41]. Filtering and segmentation were performed on the whole investigated volume, whereas the more computationally intensive steps of the quantitative image analysis have been performed on a suitable volume of interest (VOI). The significance/representativeness of the VOIs has been assessed by determining the representative elementary volumes (REVs) for each sample. This approach, which has become standard in the analysis of SR- μ CT data of porous media [42], is based on the definition of the REV as the volume in which the measurement of a sample property (i.e. porosity) is scale independent and accurately represents a larger volume, that is, the whole investigated sample [43]. The REV was identified through plots of porosity, calculated on progressively larger concentric cubic volumes (an example is provided as Online Resource 1), as already showed elsewhere [42, 44, 45]. A larger VOI of 1280 \times 1280 \times 1280 voxels, corresponding to a volume of 1.529 mm³, was chosen. For a meaningful description of the VOI, voids with volume less than 27 voxels (volume < 19.7 μm^3) have been excluded from the quantitative analysis. The parameters obtained from the quantitative image analysis of each VOI were: porosity [Φ (%)]; surface area per unit volume [S_V (mm⁻¹)]; fractal dimension (D_F) according to the fractal theory [46], employing the box-counting method; distribution of pore volumes; connectivity density [CD (mm⁻³)]. CD is a

scalar value derived from the skeleton of the connected pore network representing the number of redundant connections normalized to the total sample volume. The skeletonization is a 1D representation of 3D objects which preserves their topology [38, 47]. This computationally intensive process has been conducted by applying the GFV algorithm [48].

Scanning electron microscope (SEM) analysis

SEM images were collected from the freshly fractured surface of the specimens. Samples were mounted on aluminium stubs and coated with 5 nm thick gold film. Observations have been conducted with a FEI QUANTA FEG 450 instrument, equipped with an energy-dispersive detector, at 20 kV accelerating voltage. A gaseous backscatter electron detector working at 200 Pa pressure was chosen, in order to limit the water loss from the samples.

Results

Figure 1 depicts axial 2D SR- μ CT views after tomographic reconstruction of the specimens with different water content aged 15 days.

Phase composition has been controlled with X-ray powder diffraction (diffraction spectra are reported in Online Resource 2), and the presence of only MKP as crystalline reaction product has been confirmed, in agreement with results from MPC samples with different w/s ratio [8, 16, 18]. Previous results of quantitative phase analysis indicated that MKP largely prevails over the amorphous phase [13, 14, 18]. The compact microstructure exhibited by sample MPC_044_15d confirms that, at low w/s ratio, the crystals are densely packed and embedded in the amorphous phase from which they crystallized [16, 17, 25, 49]. Few large pores (size $> 200 \mu\text{m}$) of irregular shape are observed.

As the w/s ratio increased, the number of voids increased as well. In section, pores are more irregular, and the microstructure appears less compact as more elongated features are present in the sample volume. The outline of these features is compatible with the crystal habit of MKP crystals, which ranges from acicular/elongated to platelet-like [27, 50]. This indicates that the number of euhedral to subhedral MKP crystals increases with w/s ratio.

The 3D visualization of a VOI at different w/s ratio, reported in Fig. 2, clearly illustrates this evolution. In the samples MPC_207_15d and MPC_400_15d, the voids are more pervasive and crystals likely allowed to grow larger. The number of spherical to sub-spherical pores, previously attributed to air entrapment during mixing [9], is insignificant. Increasing w/s , the crystal network becomes sparser and individuals can be better distinguished because they are less packed and more isolated.

Figure 3a, b illustrates an example of 2D axial views after segmentation, obtained from the sample MPC_051 after 1 h and 12 h. The two pictures identify the same portion of sample and are very similar, indicating small changes in porosity. Figure 3c depicts a detail of the image obtained by subtracting the previous two. The formation of new small pores (white phase in figure) can be observed.

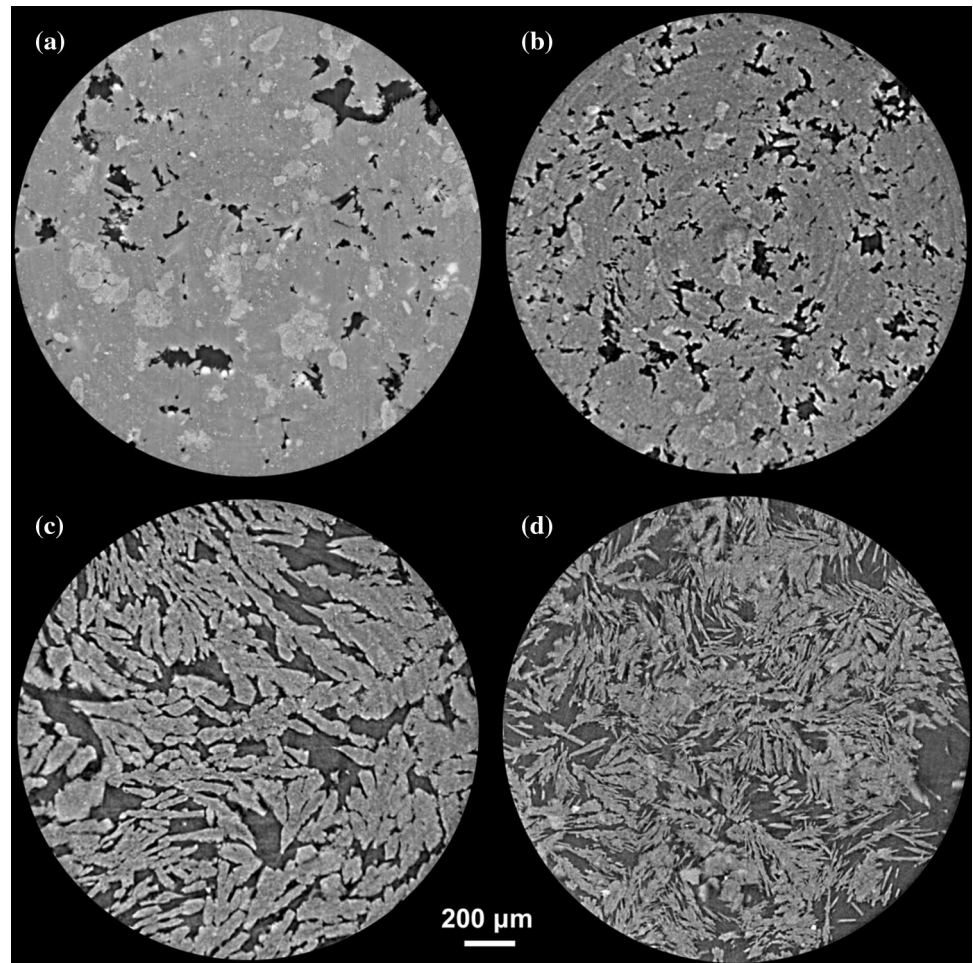
Results from quantitative image analysis are summarized in Table 1. They reflect the sample features in the range of sizes made accessible by the resolution of the experiment.

The increase in water content of the mix above the stoichiometric amount, increased the values of porosity Φ and specific surface area S_V . The latter also reflects the increased complexity of pore shape mentioned above, which is accompanied by an increasing complexity of the pore network, as testified by higher CD (from 355 to $> 10000 \text{ mm}^{-3}$). Figure 4 shows an example of 3D volume rendering including the skeletonized volume. A more complex skeleton increasing w/s ratio is evident.

The fractal dimension D_F is obtained by applying the concepts of fractal geometry to describe the pore network, in analogy with several examples in rocks, cements and ceramics [28, 29, 51–53]. The theoretical foundations of this approach can be found elsewhere [54, 55]. In this study, D_F can be simply considered as an indicator of roughness of the pore surface [56] which can assume values from 2 (smooth surface) to 3 (irregular or rough surface). In agreement with the other parameters of the quantitative image analysis and in parallel with the increasing complexity of the pore–matrix interface, D_F increases with w/s .

A visual representation of the pore size distribution, expressed as incremental volume plotted against the pore volume, for samples produced with different w/s ratio, is reported in Fig. 5a. The sample with the lowest w/s ratio exhibits a broad distribution which extends to large volumes ($> 10^5 \mu\text{m}^3$). As the

Figure 1 SR- μ CT axial slices of sample MPC_044_15d (a), MPC_100_15d (b), MPC_207_15d (c) and MPC_400_15d (d).



w/s ratio increases, the distribution narrows and the maximum shifts towards smaller volumes. With w/s ratio 4.0, the porosity is mostly contributed by pores with volume between 100 and 2000 μm^3 , corresponding to diameter D of the sphere having the same volume, between 5.8 and 15.6 μm . Since the porosity also increases (this aspect cannot be appreciated in Fig. 5, since the sum of the contributions is 100% for each curve), excess water results in the development of more pores, smaller in size, more interconnected and with more complex pore shape (Table 1).

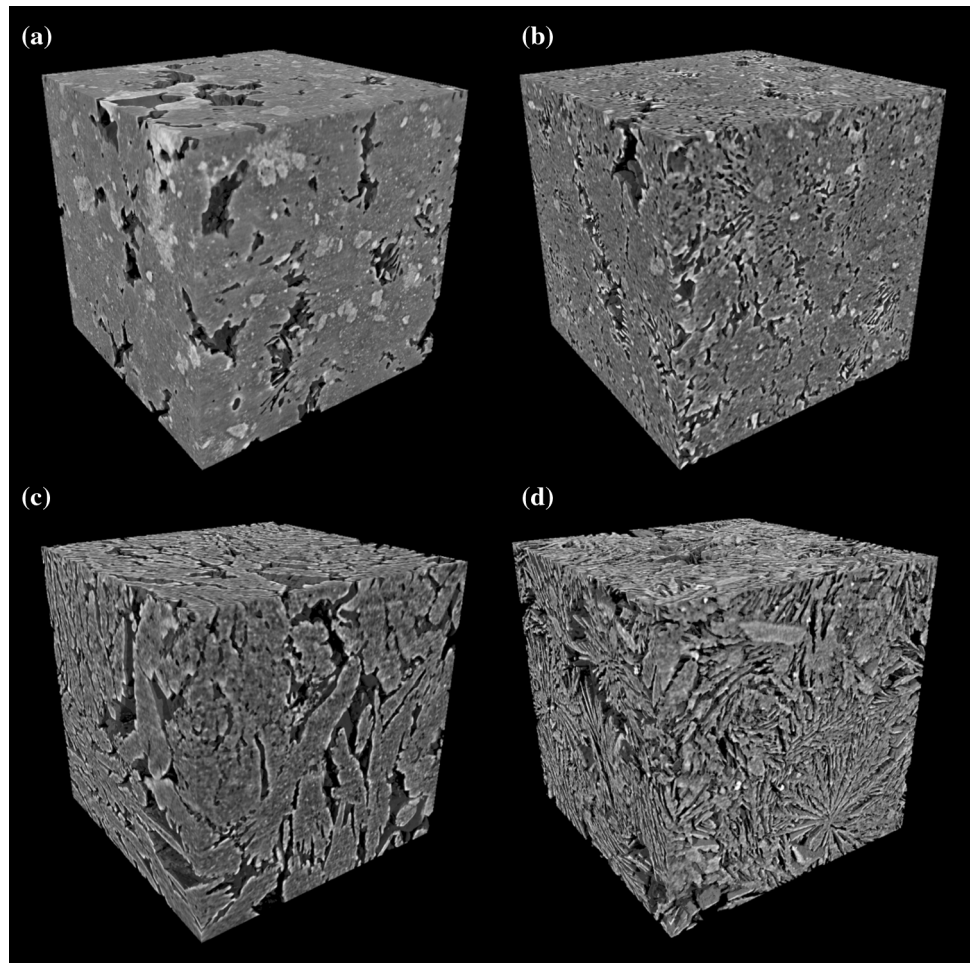
The time evolution of the distribution for the sample MPC_051 is illustrated in Fig. 5b. As for the other results of quantitative image analysis reported in Table 1, most of the changes are observed between 1 and 4 h. They consist in a shift of the maximum of the distribution towards smaller pore volumes (from 5×10^3 to $1 \times 10^3 \mu\text{m}^3$) and a decrease in the contribution from pores larger than $4 \times 10^4 \mu\text{m}^3$

($D > 42 \mu\text{m}$). Notably, this does not coincide with a decrease in porosity, but rather to a small increase (Table 1). The detected porosity and S_V remain slightly higher than at 1 h, even after 12 h. An evidence which agrees with the two snapshots in Fig. 3, which show some new pores with $D < 25 \mu\text{m}$ detected at 12 h. The results reported in Table 1 coherently indicate a porosity and a connectivity density intermediate between samples with w/s ratio 0.44 and 1.0 aged 15 days. The same does not occur for S_V , which is higher than in sample MPC_100_15d. This might suggest that the slight decrease in porosity and S_V , observed between 4 and 12 h, continues for longer times.

Figure 6 reports examples of SEM micrographs collected from the fractured surface of the specimens.

When no excess water was employed (sample MPC_044_15d), the microstructure appears more compact. Pores are isolated and occasionally larger than 20 μm , as illustrated in Fig. 6a. MKP crystals

Figure 2 Gallery of 3D volume renderings (VOI = 1.529 mm³) of the MPC microstructure for sample MPC_044_15d (a), MPC_100_15d (b), MPC_207_15d (c) and MPC_400_15d (d).



exhibiting two habits, tabular and more elongated/acicular, are intimately mixed together. In the matrix, they are roughly 5 μm in size (as indicated by arrow in Fig. 6a), but in correspondence with the large pores, where they are clearly distinguishable, they grew bigger protruding into the pore volume. As the w/s ratio increases, the microstructure becomes less compact, MKP crystals grow on average larger ($> 50 \mu\text{m}$) and the tabular crystal habit prevails. This suggests a relationship between the crystal size and shape, and the space available for the crystals to grow. At high w/s ratio (samples MPC_207_15d and MPC_400_15d), small crystals of MKP ($< 5 \mu\text{m}$), whose chemistry has been confirmed by EDS analysis (Online Resource 3), are also observed on the surface of the large tabular ones shown in Fig. 6c, d. Their diffuse presence in sample MPC_207_15d explains why, with SR- μCT , MKP individuals appear less sharply defined in this sample (Figs. 1c, 2c).

Discussion

The observed relationship between mix formulation and development of microstructure will be interpreted in the light of the existing theories on reaction mechanisms. In this view should also be intended the use of a wide range of w/s ratio. As already showed, formulations with very different water contents may help to gain insights into the process leading to the development of properties in this class of ceramics [16, 19–23].

It has to be noted that, when comparing with data from the literature, the w/s ratio is a simplified way to describe the MPC formulation, because of the frequent introduction of fillers and the variable MgO/KDP molar ratios employed. Nonetheless, this index still finds widespread use in the literature, and for this reason it has been adopted also in this work.

It is well known that the microstructure of MPCs develops very quickly. Reaction rates slow down after the first hour; by this time, a compact solid has

Figure 3 Examples of segmented SR- μ CT slices of sample MPC_051_1h (a) and MPC_051_12h (b). Detail of the image obtained by subtraction of the previous two (c), evidencing new pores (white phase) formed after 12 h.

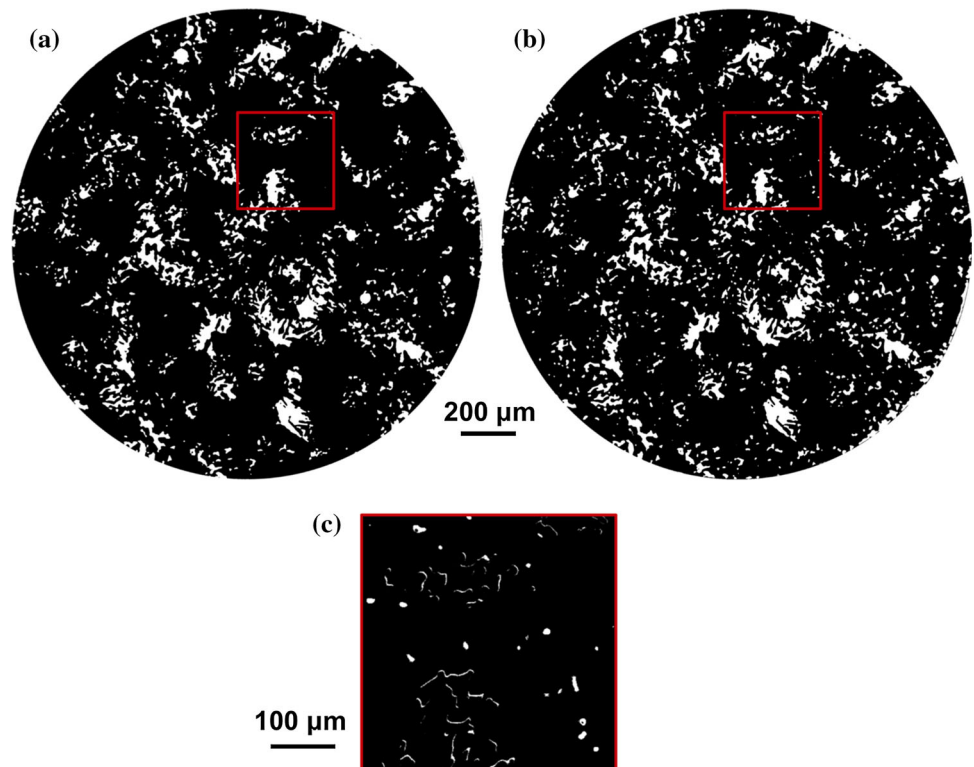


Table 1 Results of quantitative image analysis of the pore network for the investigated samples

Sample	$\Phi/\%$	S_V/mm^{-1}	CD/mm^{-3}	D_F
MPC_044_15d	7.8	11.3	355	2.40
MPC_100_15d	14.2	34.3	4121	2.57
MPC_207_15d	27.6	41.5	11302	2.70
MPC_400_15d	45.1	81.8	10247	2.82
MPC_051_1h	12.9	36.0	2447	2.55
MPC_051_4h	13.8	40.2	2405	2.57
MPC_051_9h	13.6	39.4	2453	2.57
MPC_051_12h	13.5	38.6	2361	2.57

already formed [50, 57]. Recent works pointed to amorphous gel-like phases as first reaction products [13, 14, 18, 57, 58], in agreement with previous models of ceramic formation [59, 60]. It has been proposed that the amorphous fraction forms thanks to the high degree of supersaturation established in solution in proximity of the MgO grains [50, 61]. This process is later hindered by the increase in the pH of the solution and the isolation of MgO particles due to the development of the reaction products. It follows that the amount of water in the starting mix is expected to affect the kinetics of the setting reaction,

by modifying the supersaturation conditions in solution, and, consequently, the amount of MKP formed at each time. These aspects are still poorly understood.

The results presented in the previous section indicate that the increase in w/s ratio above the stoichiometric value brings about a net increase in porosity of the ceramic body. For the formulations with $w/s \leq 1.00$, the pore size interested by this increase in porosity ($7.2 \mu\text{m} < D < 15.6 \mu\text{m}$) is larger than the one detected with MIP in some previous studies [7, 24, 25]. But a porous structure with pores of size around $10 \mu\text{m}$, with detriment for the continuity of the microstructure, has been reported to form when excess water with respect to the stoichiometric amount (i.e. $w/s = 0.44$, in our case) was employed [60]. In that work, the samples spanned a range in water corresponding to our w/s $0.44 \div 0.7$, but also contained a large amount of unreacted solid powder. Nonetheless, this ‘critical’ pore size is in good agreement with the one observed in our study. It is worth noting that contribution from pores with D larger than $40\text{--}70 \mu\text{m}$ falls to zero by increasing water content, which seems at variance with the commonly accepted view that water segregation leads to the formation of inhomogeneities at large

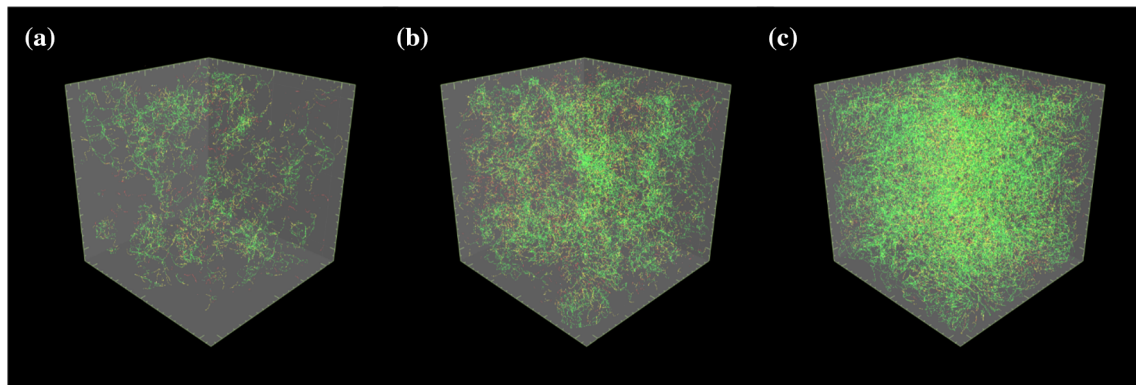


Figure 4 Skeletonized volumes ($VOI = 1.529 \text{ mm}^3$) from samples MPC_044_15d (a), MPC_100_15d (b) and MPC_400_15 (c).

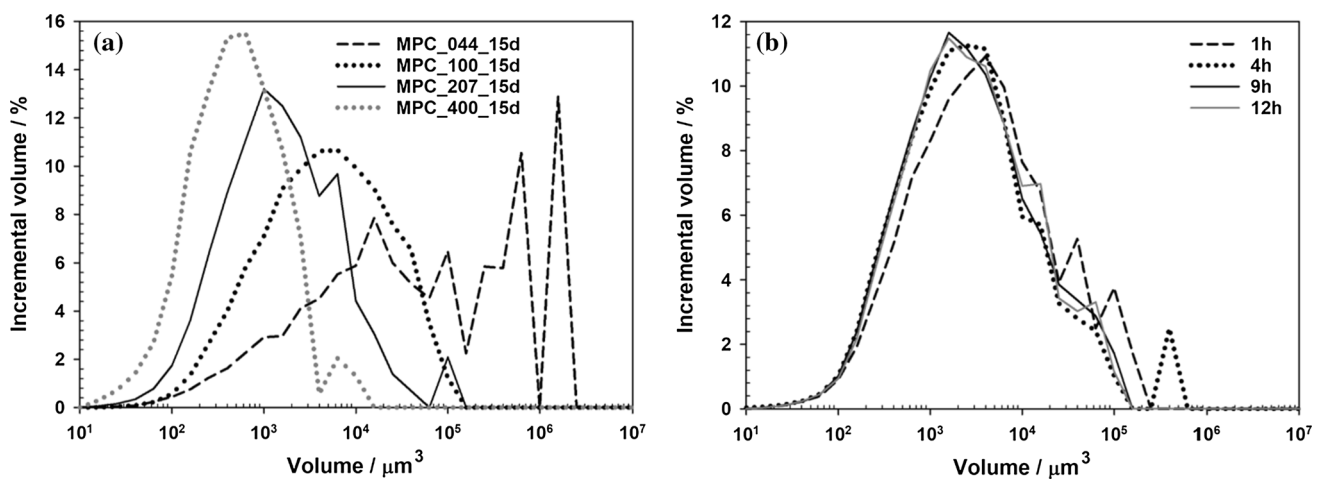
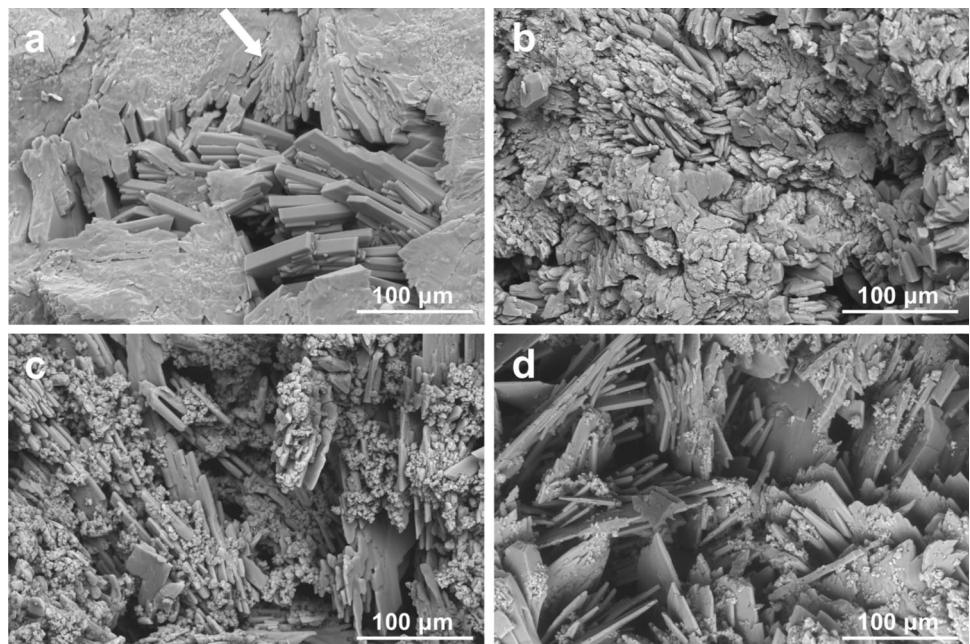


Figure 5 Incremental volume distribution for samples with different w/s ratio (a) and for sample MPC_051 at increasing times (b), as indicated.

Figure 6 Gallery of SEM micrographs from the fractured surface of samples MPC_044_15d (a), MPC_100_15d (b), MPC_207_15d (c) and MPC_400_15d (d).



scale. For the formulations adopted in this study, the absence of very large pores can be explained by considering that in less dense systems, containing more water, MKP crystals are allowed to grow larger (as illustrated in Figs. 1, 2, 6), with the net result of a more 'fragmented' pore volume. This may also lead to a reduction in the average pore size, producing a more complex pore network of higher specific surface area and connectivity, as testified by the parameters reported in Table 1.

The growth of larger crystals of magnesium ammonium phosphate (isostructural with MKP) increasing w/s ratio has been reported in mortars obtained using ammonium phosphate in place of KDP and with addition of inert fillers [60]. The increase in water content of the mix also favoured the formation of tabular over needle-like crystals [24]. Similar change in crystal habit was observed in solution, when decreasing the degree of supersaturation [62]. These facts were considered an indirect evidence of crystallization via a through-solution process, a mechanism alternative to the one involving a gel-like precursor. In fact, it is plausible that, in diluted systems, leaving the kinetic path, the reaction follows a different mechanism. The crystallization of metastable intermediate phases at high water contents (w/s ratios between 5 and 100) [16, 20–22] agrees with this view. For water contents in the range covered in the present experiment, after 30 min MKP was the only crystalline product detected [16, 22], as confirmed by the obtained X-ray powder diffraction (Online Resource 2) and SEM results.

Crystallization and growth of MKP from the amorphous precursor likely predominates when the excess of water in the mix is low, as in the sample MPC_051. In such 'dense' systems, the time evolution of the microstructure can be explained considering that crystalline MKP, owing to its peculiar crystal habit (from tabular to acicular [50]), fills the space in a different way with respect to the amorphous phase. Moreover, it can be argued that MKP possesses a slightly higher density, since amorphous materials are known to be less dense than the corresponding crystalline solids [63]. The small increase in porosity observed between 1 and 4 h might be thus explained by considering that crystal growth produces some new voids (still observed after 12 h, as shown in Fig. 3c). As the material ages, amorphous is replaced by MKP at slower rate and without big microstructural changes. The crystal growth in the large pores

results in a limited reduction in porosity and in the shift of the distribution towards smaller pore volumes (Fig. 5b). The very small shrinkage of MPCs ($2.6\text{--}3.4 \times 10^{-5}$ after 28 days [64, 65]) seems in agreement with crystallization of a denser phase (MKP) counterbalanced by the appearance of additional porosity.

It can be speculated that MPC microstructure is controlled by MKP crystallization on the one side and water segregation on the other. When the water is in stoichiometric amount (according to Eq. 1) or in small excess, high supersaturation levels are attained in proximity of MgO grains, the reaction occurs far from equilibrium (kinetically driven) and condensation of phosphate groups and hydrated Mg complexes [66] produce large amount of amorphous phase, filling the volume [18]. Upon crystallization, new pores will form because of the higher density of MKP. As the amount of water increases, a small number of new pores will develop this way, but the volume of water 'pockets' in the sample increases, allowing MKP crystals to grow larger. Lower supersaturation degrees are attained, and the through-solution crystallization mechanism will be favoured. In this view, the presence of small excess of water in the mix in the sample MPC_051 might explain why only a limited number of new pores formed in time.

Conclusions

For the first time, the 3D microstructure of magnesium potassium phosphate ceramics has been investigated in a fully non-invasive fashion by synchrotron X-ray computed microtomography in phase-contrast mode to derive information on the reaction mechanisms. Quantitative image analysis has been performed on samples with different water content, and the results can be summarized as follows:

- The increase in water content of the mix yielded an increase in detected porosity, due to the segregation of water in excess with respect to the stoichiometry of the setting reaction. As a consequence, the interlocked lath-shaped microstructure, constituted by MKP crystals, loses compactness. This is well reflected in the dramatic increase in the CD of the pore network. Moreover, the complexity of the pore shape increased, since

crystals were allowed to grow larger in the water ‘pockets’ developed in the sample volume.

- The growth of large crystals explains why, by increasing the water content of the mix, porosity is mostly contributed by smaller ($7.2 \mu\text{m} < D < 15.6 \mu\text{m}$) pores, with a decrease in the fraction of larger ($D > 50 \mu\text{m}$) ones.
- The increase in water content favours crystallization of platelet over elongated/acicular crystals. This change in crystal habit is likely related to a change in reaction mechanism. The formation of a gel-like amorphous precursor is hindered and substituted by a through-solution mechanism.
- It is proposed that in MPCs the porosity develops thanks to two contributions. The first is the crystallization of MKP from amorphous, which predominates in relatively ‘dense’ systems (with stoichiometric water or in low excess), and the second is the water segregation, which predominates at higher water content. According to the results of microstructural time evolution, the first process causes the porosity to increase due to the density mismatch between the amorphous phase and MKP, and their different way to fill the volume.

Acknowledgments

This research was partially supported by the Project No. LO1219 under the Ministry of Education, Youth and Sports National sustainability programme I of Czech Republic. The authors acknowledge the CERIC-ERIC Consortium for the access to synchrotron radiation computed microtomography facilities at Elettra and financial support.

Funding

Funding was provided by Ministerstvo Školství, Mládeže a Tělovýchovy (Grant No. LO1219).

Compliance with ethical standards

Conflict of interest The authors declare no conflict of interest.

Electronic supplementary material: The online version of this article (<https://doi.org/10.1007/s108>

[53-018-3113-7](https://doi.org/10.1007/s108)) contains supplementary material, which is available to authorized users.

Open Access This article is distributed under the terms of the Creative Commons Attribution 4.0 International License (<http://creativecommons.org/licenses/by/4.0/>), which permits unrestricted use, distribution, and reproduction in any medium, provided you give appropriate credit to the original author(s) and the source, provide a link to the Creative Commons license, and indicate if changes were made.

References

- [1] Ostrowski N, Roy A, Kumta PN (2016) Magnesium phosphate cement systems for hard tissue applications: a review. *ACS Biomater Sci Eng* 2:1067–1083. <https://doi.org/10.1021/acsbiomaterials.6b00056>
- [2] Neiman R, Sarma AC (1980) Setting and thermal reactions of phosphate investments. *J Dent Res* 59:1478–1485. <https://doi.org/10.1177/00220345800590090401>
- [3] Covill A, Hyatt NC, Hill J, Collier NC (2011) Development of magnesium phosphate cements for encapsulation of radioactive waste. *Adv Appl Ceram* 110:151–156. <https://doi.org/10.1179/1743676110Y.0000000008>
- [4] Seehra SS, Gupta S, Kumar S (1993) Rapid setting magnesium phosphate cement for quick repair of concrete pavements—characterisation and durability aspects. *Cem Concr Res* 23:254–266. [https://doi.org/10.1016/0008-8846\(93\)90090-V](https://doi.org/10.1016/0008-8846(93)90090-V)
- [5] Ibrahim HA, Sibak A, Abadir MF (2011) Preparation and characterization of chemically bonded phosphate ceramics (CBPC) for encapsulation of harmful waste. *J Am Sci* 7:543–548
- [6] Li Y, Sun J, Li J, Shi T (2015) Effects of fly ash, retarder and calcination of magnesia on properties of magnesia–phosphate cement. *Adv Cem Res* 27:373–380. <https://doi.org/10.1680/adcr.14.00029>
- [7] Ma H, Xu B, Liu J et al (2014) Effects of water content, magnesia-to-phosphate molar ratio and age on pore structure, strength and permeability of magnesium potassium phosphate cement paste. *Mater Des* 64:497–502. <https://doi.org/10.1016/j.matdes.2014.07.073>
- [8] Xu B, Ma H, Li Z (2015) Influence of magnesia-to-phosphate molar ratio on microstructures, mechanical properties and thermal conductivity of magnesium potassium phosphate cement paste with large water-to-solid ratio. *Cem Concr Res* 68:1–9. <https://doi.org/10.1016/j.cemconres.2014.10.019>

- [9] Hall DA, Stevens R, El Jazairi B (1998) Effect of water content on the structure and mechanical properties of magnesia-phosphate cement mortar. *J Am Ceram Soc* 81:1550–1556
- [10] Walling SA, Provis JL (2016) Magnesia-based cements: a journey of 150 years, and cements for the future? *Chem Rev* 116:4170–4204. <https://doi.org/10.1021/acs.chemrev.5b00463>
- [11] Wilson A, Nicholson JW (1993) Acid-base cements. Cambridge University Press, Cambridge
- [12] Xing F, Ding Z, Li Z-J (2011) Study of potassium-based magnesium phosphate cement. *Adv Cem Res* 23:81–87. <https://doi.org/10.1680/adcr.9.00030>
- [13] Viani A, Radulescu A, Pérez-Estébanez M (2015) Characterisation and development of fine porosity in magnesium potassium phosphate ceramics. *Mater Lett* 161:628–630. <https://doi.org/10.1016/j.matlet.2015.09.056>
- [14] Viani A, Gualtieri AF (2014) Preparation of magnesium phosphate cement by recycling the product of thermal transformation of asbestos containing wastes. *Cem Concr Res* 58:56–66. <https://doi.org/10.1016/j.cemconres.2013.11.016>
- [15] Pérez-Estébanez M, Mácová P, Šašek P, Viani A, Gualtieri AF (2014) Mg-phosphate ceramics produced from the product of thermal transformation of cement-asbestos. *J Pol Miner Eng Soc* 15:187–192
- [16] Xu B, Lothenbach B, Leemann A, Winnefeld F (2018) Reaction mechanism of magnesium potassium phosphate cement with high magnesium-to-phosphate ratio. *Cem Concr Res* 108:140–151. <https://doi.org/10.1016/j.cemconres.2018.03.013>
- [17] Ding Z, Dong B, Xing F et al (2012) Cementing mechanism of potassium phosphate based magnesium phosphate cement. *Ceram Int* 38:6281–6288. <https://doi.org/10.1016/j.ceramint.2012.04.083>
- [18] Viani A, Sotiriadis K, Šašek P, Appavou M-S (2016) Evolution of microstructure and performance in magnesium potassium phosphate ceramics: role of sintering temperature of MgO powder. *Ceram Int* 42:16310–16316. <https://doi.org/10.1016/j.ceramint.2016.07.182>
- [19] Qiao F, Chau CK, Li Z (2012) Calorimetric study of magnesium potassium phosphate cement. *Mater Struct* 45:447–456. <https://doi.org/10.1617/s11527-011-9776-z>
- [20] Lahalle H, Cau Dit Coumes C, Mercier C et al (2018) Influence of the w/c ratio on the hydration process of a magnesium phosphate cement and on its retardation by boric acid. *Cem Concr Res* 109:159–174. <https://doi.org/10.1016/j.cemconres.2018.04.010>
- [21] Abbona F, Lundager Madsen HE, Boistelle R (1982) Crystallization of two magnesium phosphates, struvite and newberyite: effect of pH and concentration. *J Cryst Growth* 57:6–14. [https://doi.org/10.1016/0022-0248\(82\)90242-1](https://doi.org/10.1016/0022-0248(82)90242-1)
- [22] Le Rouzic M, Chaussadent T, Platret G, Stefan L (2017) Mechanisms of k-struvite formation in magnesium phosphate cements. *Cem Concr Res* 91:117–122. <https://doi.org/10.1016/j.cemconres.2016.11.008>
- [23] Moseke C, Saratsis V, Gbureck U (2011) Injectability and mechanical properties of magnesium phosphate cements. *J Mater Sci Mater Med* 22:2591–2598. <https://doi.org/10.1007/s10856-011-4442-0>
- [24] Abdelrazig BEI, Sharp JH, El-Jazairi B (1989) The microstructure and mechanical properties of mortars made from magnesia-phosphate cement. *Cem Concr Res* 19:247–258. [https://doi.org/10.1016/0008-8846\(89\)90089-6](https://doi.org/10.1016/0008-8846(89)90089-6)
- [25] Ding Z, Li Z (2005) Effect of aggregates and water contents on the properties of magnesium phospho-silicate cement. *Cem Concr Compos* 27:11–18. <https://doi.org/10.1016/j.cemconcomp.2004.03.003>
- [26] Viani A, Mácová P (2018) Polyamorphism and frustrated crystallization in the acid-base reaction of magnesium potassium phosphate cements. *CrystEngComm* 20:4600–4613. <https://doi.org/10.1039/c8ce00670a>
- [27] Le Rouzic M, Chaussadent T, Stefan L, Saillio M (2017) On the influence of Mg/P ratio on the properties and durability of magnesium potassium phosphate cement pastes. *Cem Concr Res* 96:27–41. <https://doi.org/10.1016/j.cemconres.2017.02.033>
- [28] Maire E, Withers PJ (2014) Quantitative X-ray tomography. *Int Mater Rev* 59:1–43. <https://doi.org/10.1179/1743280413Y.0000000023>
- [29] Anovitz LM, Cole DR (2015) Characterization and analysis of porosity and pore structures. *Rev Mineral Geochem* 80:61–164. <https://doi.org/10.2138/rmg.2015.80.04>
- [30] Zhang J, Scherer GW (2011) Comparison of methods for arresting hydration of cement. *Cem Concr Res* 41:1024–1036. <https://doi.org/10.1016/j.cemconres.2011.06.003>
- [31] Wheeler R, Frost G (1955) A comparative study of the dehydration kinetics of several hydrated salts. *Can J Chem* 33:546–561
- [32] Wilkins SW, Gureyev TE, Gao DC et al (1996) Phase-contrast imaging using polychromatic hard X-rays. *Nature* 384:335–338
- [33] Cloetens P, Barrett R, Baruchel J et al (1996) Phase objects in synchrotron radiation hard x-ray imaging. *J Phys D Appl Phys* 29:133–146. <https://doi.org/10.1088/0022-3727/29/1/023>
- [34] Brun F, Pacilè S, Accardo A et al (2015) Enhanced and flexible software tools for X-ray computed tomography at the Italian synchrotron radiation facility Elettra. *Fundam Inform* 141:233–243. <https://doi.org/10.3233/FI-2015-1273>

- [35] Brun F, Massimi L, Fratini M et al (2017) SYRMEP Tomo Project: a graphical user interface for customizing CT reconstruction workflows. *Adv Struct Chem Imaging* 3:4. <https://doi.org/10.1186/s40679-016-0036-8>
- [36] Kak AC, Slaney M (2001) Tomographic imaging with diffracting sources. In: *Principles of computerized tomographic imaging*. Society for Industrial and Applied Mathematics, pp 203–274
- [37] Paganin D, Mayo SC, Gureyev TE et al (2002) Simultaneous phase and amplitude extraction from a single defocused image of a homogeneous object. *J Microsc* 206:33–40. <https://doi.org/10.1046/j.1365-2818.2002.01010.x>
- [38] Brun F, Mancini L, Kasae P et al (2010) Pore3D: a software library for quantitative analysis of porous media. *Nucl Instrum Methods Phys Res Sect A Accel Spectrom Detect Assoc Equip* 615:326–332. <https://doi.org/10.1016/j.nima.2010.02.063>
- [39] Schindelin J, Arganda-Carreras I, Frise E et al (2012) Fiji: an open-source platform for biological-image analysis. *Nat Methods* 9:676–682. <https://doi.org/10.1038/nmeth.2019>
- [40] Weickert J (1998) *Anisotropic diffusion in image processing*. Teubner-Verlag, Stuttgart
- [41] Otsu N (1979) A threshold selection method from gray-level histograms. *IEEE Trans Syst Man Cybern* 9:62–66. <https://doi.org/10.1109/TSMC.1979.4310076>
- [42] Costanza-Robinson, Estabrook BD, Fouhey DF (2011) Representative elementary volume estimation for porosity, moisture saturation, and air-water interfacial areas in unsaturated porous media: data quality implications. *Water Resour Res*. <https://doi.org/10.1029/2010wr009655>
- [43] Bear J (1975) Dynamics of fluids in porous media. *Soil Sci* 120:162–163. <https://doi.org/10.1097/00010694-197508000-00022>
- [44] Al-Raoush R, Papadopoulos A (2010) Representative elementary volume analysis of porous media using X-ray computed tomography. *Powder Technol* 200:69–77. <https://doi.org/10.1016/j.powtec.2010.02.011>
- [45] Mostaghimi P, Blunt MJ, Bijeljic B (2013) Computations of absolute permeability on micro-CT images. *Math Geosci* 45:103–125. <https://doi.org/10.1007/s11004-012-9431-4>
- [46] Mandelbrot B (1977) *Fractals: form, chance, and dimension*. W.H. Freeman & Co, London
- [47] Lindquist WB, Venkatarangan A (1999) Investigating 3D geometry of porous media from high resolution images. *Phys Chem Earth Part A Solid Earth Geod* 24:593–599. [https://doi.org/10.1016/S1464-1895\(99\)00085-X](https://doi.org/10.1016/S1464-1895(99)00085-X)
- [48] Brun F, Dreossi D (2010) Efficient curve-skeleton computation for the analysis of biomedical 3d images—biomed 2010. *Biomed Sci Instrum* 46:475–480
- [49] Chau CK, Qiao F, Li Z (2011) Microstructure of magnesium potassium phosphate cement. *Constr Build Mater* 25:2911–2917. <https://doi.org/10.1016/j.conbuildmat.2010.12.035>
- [50] Viani A, Pérez-Estébanez M, Pollastri S, Gualtieri AF (2016) In situ synchrotron powder diffraction study of the setting reaction kinetics of magnesium-potassium phosphate cements. *Cem Concr Res* 79:344–352. <https://doi.org/10.1016/j.cemconres.2015.10.007>
- [51] Winslow DN, Bukowski JM, Francis Young J (1994) The early evolution of the surface of hydrating cement. *Cem Concr Res* 24:1025–1032. [https://doi.org/10.1016/0008-8846\(94\)90025-6](https://doi.org/10.1016/0008-8846(94)90025-6)
- [52] Ling EJY, Servio P, Kietzig A-M (2016) Fractal and lacunarity analyses: quantitative characterization of hierarchical surface topographies. *Microsc Microanal* 22:168–177. <https://doi.org/10.1017/S1431927615015561>
- [53] Navarre-Sitchler A, Brantley SL, Rother G (2015) How porosity increases during incipient weathering of crystalline silicate rocks. *Rev Mineral Geochem* 80:331–354. <https://doi.org/10.2138/rmg.2015.80.10>
- [54] Jelinek HF, Jones CL, Warfel MD et al (2006) Understanding fractal analysis? The case of fractal linguistics. *Complex* 3:66–73. <https://doi.org/10.1159/000094189>
- [55] Stanley HE (1996) Fractals and multifractals: the interplay of physics and geometry. In: Bunde A, Havlin S (eds) *Fractals and disordered systems*. Springer, Berlin, pp 1–58
- [56] Pfeifer P, Avnir D (1983) Chemistry in noninteger dimensions between two and three. I. Fractal theory of heterogeneous surfaces. *J Chem Phys* 79:3558–3565. <https://doi.org/10.1063/1.446210>
- [57] Taris A, Grosso M, Brundu M et al (2017) Application of combined multivariate techniques for the description of time-resolved powder X-ray diffraction data. *J Appl Crystallogr* 50:451–461. <https://doi.org/10.1107/S1600576717001753>
- [58] Viani A, Mali G, Mácová P (2017) Investigation of amorphous and crystalline phosphates in magnesium phosphate ceramics with solid-state ^1H and ^{31}P NMR spectroscopy. *Ceram Int* 43:6571–6579. <https://doi.org/10.1016/j.ceramint.2017.02.087>
- [59] Wilson AD, Nicholson JW (1993) *Acid-base cements. Their biomedical and industrial applications*. Cambridge University Press, Cambridge
- [60] Hall DA, Stevens R, El Jazairi B (1998) Effect of water content on the structure and mechanical properties of magnesia-phosphate cement mortar. *J Am Ceram Soc* 56:1550–1556
- [61] Viani A, Zbiri M, Bordallo HN et al (2017) Investigation of the setting reaction in magnesium phosphate ceramics with

- quasielastic neutron scattering. *J Phys Chem C* 121:11355–11367. <https://doi.org/10.1021/acs.jpcc.7b01396>
- [62] Abbona F, Boistelle R (1979) Growth morphology and crystal habit of struvite crystals ($\text{MgNH}_4\text{PO}_4 \cdot 6\text{H}_2\text{O}$). *J Cryst Growth* 46:339–354. [https://doi.org/10.1016/0022-0248\(79\)90082-4](https://doi.org/10.1016/0022-0248(79)90082-4)
- [63] Navrotsky A (2004) Energetic clues to pathways to biomineralization: precursors, clusters, and nanoparticles. *Proc Natl Acad Sci* 101:12096–12101. <https://doi.org/10.1073/pnas.0404778101>
- [64] Li Y, Chen B (2013) Factors that affect the properties of magnesium phosphate cement. *Constr Build Mater* 47:977–983. <https://doi.org/10.1016/j.conbuildmat.2013.05.103>
- [65] Li J, Zhang W, Cao Y (2014) Laboratory evaluation of magnesium phosphate cement paste and mortar for rapid repair of cement concrete pavement. *Constr Build Mater* 58:122–128. <https://doi.org/10.1016/j.conbuildmat.2014.02.015>
- [66] Soudée E, Péra J (2000) Mechanism of setting reaction in magnesia-phosphate cements. *Cem Concr Res* 30:315–321. [https://doi.org/10.1016/S0008-8846\(99\)00254-9](https://doi.org/10.1016/S0008-8846(99)00254-9)